Failure to resolve inflammation contributes to juvenile onset cardiac damage in a mouse model of Duchenne Muscular Dystrophy

James S. Novak[1,2†], Amy Lischin[1,3], Prech Uapinyoying[1,4], Ravi Hindupur[1], Young Jae Moon[1,5], Surajit Bhattacharya[1], Sarah Tiufekchiev[1,6], Victoria Barone[1,3], Davi A. G. Mázala[1,7], Iteoluwakishi H. Gamu[1], Gabriela Walters[1], Jyoti K. Jaiswal[1,2†]

[1] Center for Genetic Medicine Research, Children's National Research Institute, Children's National Research and Innovation Campus, Children's National Hospital, Washington, D.C., 20012, USA

[2] Departments of Pediatrics and Genomics and Precision Medicine, The George Washington University School of Medicine and Health Sciences, Washington, D.C., 20037, USA

[3] Columbian College of Arts and Sciences, The George Washington University, Washington, D.C. 20052, USA.

[4] Neuromuscular and Neurogenetic Disorders of Childhood Section, National Institute of Neurological Disorders and Stroke, National Institutes of Health, Bethesda, MD, USA.

[5] Department of Biochemistry and Orthopaedic Surgery, Jeonbuk National University Medical School and Hospital, Jeonju, 54907, Republic of Korea

[6] Integrated Biomedical Sciences, The George Washington University School of Medicine and Health Sciences, Washington, D.C., 20037, USA

[7] Department of Kinesiology, College of Health Professions, Towson University, Towson, MD, 21252, USA

† Author for correspondence

Corresponding Author Address: James S. Novak (jnovak@childrensnational.org) and Jyoti K. Jaiswal (jkjaiswal@childrensnational.org); Center for Genetic Medicine Research, Children's National Research Institute, Children's National Hospital, Washington, D.C., 20012, USA

Key words: *Duchenne muscular dystrophy, cardiomyopathy, pathology, D2-mdx, B10-mdx, inflammation, inflammatory response, pro-resolution pharmacology, macrophage, macrophage migration, neutrophil, cytokine signaling, extracellular matrix remodeling, fibrosis, calcification.*

Abstract

Absence of dystrophin protein causes cardiac dysfunction in patients with Duchenne muscular dystrophy (DMD). Unlike boys with DMD, the common mouse model of DMD (B10-*mdx*) does not manifest cardiac deficits until late adulthood. This has limited our understanding of the mechanism and therapeutic approaches to target the pediatric onset of cardiac pathology in DMD. Here we show that the *mdx* mouse model on the DBA/2J genetic background (D2-*mdx*) displays juvenile-onset cardiac degeneration. Molecular and histological analysis revealed that cardiac damage in this model is linked to increased leukocyte chemotactic signaling and an inability to resolve inflammation. These deficiencies result in chronic inflammation and fibrotic conversion of the extracellular matrix (ECM) in the juvenile D2-mdx heart. To address these pathologies, we tested the utility of pro-resolution therapy to clear chronic cardiac inflammation. Use of an N-formyl peptide receptor (FPR) agonist helped physiologically resolve inflammation and mitigate the downstream events that lead to fibrotic degeneration of cardiomyocytes, preventing juvenile onset cardiac muscle loss. These results establish the utility of D2-*mdx* model to study events associated with pediatric-onset cardiac damage and demonstrates pro-resolution therapy as an alternate to anti-inflammatory therapy for treating cardiac degenerative pathology responsible for cardiomyopathy in DMD patients.

47 **Introduction**

48 Duchenne Muscular Dystrophy (DMD) is a severe and progressive muscle disease caused
49 by the absence of dystrophin protein[1, 2, 3, 4]. Dystrophin plays a crucial role in maintaining the
50 integrity of the sarcolemmal membrane by facilitating the assembly and function of the
51 dystrophin-associated protein complex, thus its absence renders skeletal muscle cells more
52 susceptible to mechanical damage, and increased muscle degeneration[5, 6, 7]. Dystrophin
53 deficiency in cardiomyocytes also increases their vulnerability to sarcolemmal damage, cell
54 death, chronic inflammation and cardiac fibrosis. These pathologies also manifest in patients
55 and lead to the thinning of the left ventricle (LV) wall, causing their progressive dilation and
56 dilated cardiomyopathy that results in heart failure[4, 8].

57 Patients with DMD experience symptoms early in life, with cardiac deficits being a major
58 contributor to premature mortality not only in DMD, but also in DMD carriers and in Becker
59 Muscular Dystrophy (BMD)[9, 10, 11]. While the common B10-*mdx* model exhibits skeletal
60 myopathy at an early age, the cardiac deficit is not evident until late adulthood[12, 13]. The advent
61 of the D2-*mdx* model identified greater disease severity and fibrosis as compared to B10-*mdx*
62 even in younger mice[14, 15, 16, 17]. Excess skeletal muscle fibrosis in the D2-*mdx* model, results
63 from an increase in transforming growth factor beta (TGFβ) signaling, and cardiac deficit is
64 reported as early as adulthood (16-weeks of age)[17, 18, 19].

65 While therapeutic approaches to address cardiac deficit in patients with dystrophin
66 deficiency are a topic of active investigation, anti-inflammatory glucocorticoids (GCs),
67 angiotensin-converting enzyme inhibitors (ACEi), and angiotensin receptor blockers (ARBs), are
68 commonly used for these patients[11, 20, 21, 22]. Anti-inflammatory therapy by GC has the longest
69 history of use in DMD patients and has mixed reports of cardiac benefit and side effect in both
70 DMD patients and mouse models[23, 24, 25, 26, 27]. An anti-inflammatory protein activated by GCs
71 that mediates the GC efficacy is Annexin A1 (AnxA1)[28, 29]. Independent of its widely known role
72 in membrane fusion, AnxA1 is required for muscle repair by regulating inflammation by way of

73 Formyl Peptide Receptor (FPR)-mediated signaling[30, 31]. In this regard, AnxA1 works similarly to
74 the endogenous pro-resolving lipid mediators Lipoxin A4, and Resolvin D1 by helping resolve
75 acute inflammation by binding the FPRs[29, 32]. This feature of AnxA1 has led to the advent of
76 natural and synthetic agonists of FPR2, that unlike GCs, reduce inflammation by promoting
77 resolution of inflammation instead of suppressing the tissue's inflammatory response[33].
78 Use of FPR2-agonists reduces acute cardiac damage in various tissue injury models
79 including myocardial infarction, where it restricts premature heart failure and restores tissue
80 function[34, 35, 36, 37, 38]. Just as endogenous FPR2 agonists, a nanomolar dose of a synthetic
81 agonist BMS-986235 also resolves chronic inflammation in preclinical models, which has led to
82 its progress to clinical studies[38] (Clinical Trial NCT03335553). This drug activates macrophage
83 transition to a pro-resolving (M2-like) state by enhancing phagocytosis and neutrophil apoptosis,
84 that regulates their chemotaxis, all of which help improve mouse survival, reduce scarring, and
85 preserve tissue[38, 39]. These are desirable features of therapies to target cardiac inflammation
86 and fibrosis associated with the cardiac pathology observed in DMD patients.
87 To understand the early onset of cardiac dysfunction in the D2-*mdx* model, we investigated
88 the factors that distinguish the pediatric initiation of cardiac dysfunction as compared with the
89 late adult onset in B10-*mdx* model. This revealed onset of cardiac pathology in juvenile (< 6-
90 weeks old) D2-*mdx* mice, and showed this is associated with excessive immune infiltration,
91 fibrotic ECM replacement, and degenerative remodeling of cardiac ventricular walls. It identified
92 increased leukocyte chemotactic signaling and failure to resolve inflammation as major
93 contributors to the initiation of cardiac pathology. To address this deficit, we test a drug-based
94 pro-resolution therapy for a preclinical evaluation as a therapeutic approach to mitigate early-
95 onset cardiac damage in DMD mouse models and patients.
96
97 **Methods.**

98 **Animals.** All animal procedures were conducted following guidelines for the care and use of
99 laboratory animals as approved by the Institutional Animal Care and Use Committee (IACUC) of
100 Children's National Research Institute (CNRI). The C57BL/10ScSn-DMD^{mdx}/J (B10-*mdx*) and
101 D2.B10-DMD^{mdx}/J mouse models of DMD were utilized for all experiments and both harbor the
102 same nonsense point mutation in exon 23 of the dystrophin (*Dmd*) gene thereby abolishing
103 dystrophin protein expression [40, 41]. The C57BL/10ScSn/J (B10-WT) and DBA2/J (D2-WT)
104 mouse models were used as age-matched, model-specific controls. Mice were obtained from
105 the Jackson Laboratory and were housed at the CNRI Comparative Medicine Unit where they
106 were provided daily monitoring, food, water and enrichment ad libitum, while being maintained
107 under 12 h light/dark cycles.
108
109 **Tissue harvesting and sample collection.** Mice were euthanized via CO_2 inhalation and
110 cervical dislocation at designated ages corresponding to specific stages of disease progression.
111 Muscles were surgically removed, mounted on cork with tragacanth gum, flash-frozen in liquid
112 nitrogen-chilled isopentane and stored at –80°C. For all assays, samples were collected from
113 matched regions of the same muscles by collecting cryosections (Leica CM1950 cryostat) for
114 RNA analyses or histology and immunostaining assays.
115
116 **RNA extraction, RNA library preparation, RNA sequencing and bioinformatic analyses.**
117 Total RNA was extracted using TRIzol RNA isolation (Life Technologies) from frozen muscle
118 samples. RNA was purified using RNeasy mini elute columns (Qiagen) and DNAse treated
119 using Turbo DNA-free kit (Invitrogen). Purified, DNAse-treated RNA was quantified by
120 NanoDrop and quality was assessed using Qbit RNA Assays (Thermofisher) and BioAnalyzer
121 nano chips (Agilent) (RIN>7.8, Average 8.3±0.32). RNAseq library preparation and sequencing
122 was performed using the TruSeq mRNA stranded kit (Illumina) and the Illumina HiSeq4000 Flow
123 Cell with an average coverage of 63.05 million read pairs per sample at 2x75 base pair read

length. The quality of the raw fastq reads from sequencer were evaluated using FastQC version 0.11.5 followed by adapter and quality trimming using Trimgalore. STAR 2.5.3a was used to map the reads to the reference mouse genome (GRCm38-mm10). The mapped reads were counted using HTSeq (version v0.11.0) with a reference genomic feature file (Gene transfer format, GTF). Overall analysis summary reports were analyzed using MultiQC v1.6. Differential gene expression analysis was performed using default parameters with Deseq2 version 1.26 (R 3.6). Visualization was performed by PCA, pheatmap, EnhancedVolcano and ggplot2 R packages. We set a threshold for $\log_2$ fold change (Log_2FC) change of greater than an absolute value of 0.6 to select for the genes with significant differential expression. Gene lists were sorted by Log_2FC (highest to lowest) to obtain the ranked list of differentially expressed genes and a p_{adj} value cutoff of 0.05 was used to assess statistical significance.

Gene Set Enrichment Analysis (GSEA). DESeq2 pairwise comparison results were filtered for 0.6 $\log_2\text{FC}$ and 0.05 adjusted p_{adj} value and exported as tab delimited rank files (.rnk) files for upload into the stand-alone desktop version of GSEA (v4.1.0). The GSEA pre-ranked analysis was used with most default parameters except the following: the Ranked list = pairwise comparison ".rnk" file, Gene sets database = "c5.bp.v7.4.symbols" (Hallmark gene sets, GO biological processes, and gene symbols) and the Chip platform = "Mouse_Gene_Symbol_Re mapping_to_Human_Orth ologs_MSigDB.v7.4.chip".

Gene ontology analysis with Cytoscape and EnrichmentMap. The GSEA pairwise comparison results were uploaded into Cytoscape (v3.9.0) and analyzed using the EnrichmentMap pipeline collection plugins (v1.1.0). Comparisons were loaded into EnrichmentMap and the AutoAnnotate function was used with the MCL Cluster Annotation algorithm set to 5 words. The results are networks of related GO terms that are grouped together into a named network based on the most common works in each GO term within.

150 Autogenerated names of networks were renamed to fix grammar and nodes arranged to
151 improve legibility. The leading-edge genes for each cluster (node) from the immune and
152 extracellular matrix networks were exported for further analysis.
153
154 **Histology and histological analyses.** Frozen muscles were removed from -80°C cryostorage
155 and sectioned at an 8 µm thickness using a Leica CM1950 cryostat chilled to -20°C, where
156 tissues were then mounted on slides and stained using Hematoxylin and Eosin (H&E), Alizarin
157 Red, Picosirius red, and Masson's Trichrome according to TREAT-NMD Standard Operating
158 Procedures (SOPs) [41]. Thresholding parameters were applied uniformly to whole cross-section
159 tiled images acquired on the Olympus VS120-S5 Virtual Slide Scanning System using CellSens
160 Version 1.13 and ImageJ FIJI Version 2.1./1.53c. For H&E-stained sections, areas of damage
161 were selected using CellSens and quantified as percent damaged tissue area per total cross-
162 sectional muscle area. For Alizarin Red stained sections, calcified areas were selected and
163 quantified using CellSens as percent calcified tissue area per total cross-sectional muscle area.
164 For Masson's Trichrome stained sections, areas of fibrosis were calculated using FIJI (Image J)
165 and reported as percent fibrosis per total cross-sectional muscle area [41].
166
167 **Immunofluorescence.** Frozen muscles were removed from -80°C cryostorage and sectioned
168 at an 8 µm thickness and mounted on slides for immunostaining procedures. Muscle sections
169 were stained with anti-F4/80 (1:100, MCA497R, Bio-Rad), anti-COL1A1 (1:100, ab21286,
170 Abcam), and anti-GAL-3 (1:100, ab76245, Abcam). First, muscle sections were fixed in ice-cold
171 PFA for 10 min, washed in PBS (0.1% Tween-20), and blocked for 1 h in PBS supplemented
172 with 10% goat serum (GeneTex), 0.1% Tween-20 (Sigma-Aldrich), and 10 mg/mL BSA (Sigma-
173 Aldrich). Then sections were incubated with primary antibodies overnight at 4°C and
174 subsequently probed with Alexa Fluor secondary antibodies, including goat anti-rat (H+L) Alexa

175 Fluor 647 (1:500, A-21247, Thermo Fisher), goat anti-rabbit (H+L) Alexa Fluor 488 (1:500, A-
176 11008, Thermo Fisher), and goat anti-rabbit (H+L) Alexa Fluor 568 (1:500, A-11011, Thermo
177 Fisher). Sections were counterstained with wheat germ agglutinin (WGA) Alexafluor-647 (1:500,
178 W32466, Thermo Fisher) to delineate cardiomyocytes and ProLong Gold Antifade with DAPI
179 (P36935, Thermo Fisher) for nuclear staining.
180
181 **Gene expression analysis.** Hearts from juvenile and adult dystrophic mice were used to
182 perform gene expression analysis. In brief, total RNA was extracted from muscle samples by
183 standard TRIzol (Life Technologies) isolation. Purified RNA (1000ng) was reverse-transcribed
184 using Random Hexamers and High-Capacity cDNA Reverse Transcription Kit (Thermo Fisher
185 Scientific). The mRNAs were then quantified using individual TaqMan assays on an ABI
186 QuantStudio 7 Real-Time PCR machine (Applied Biosystems) using TaqMan Fast Advanced
187 Master Mix (Thermo Fisher Scientific). Specific mRNA transcript levels were quantified using
188 individual TaqMan assays (Thermo Fisher) specific for each mRNA target, including Ccl8
189 (Mm01297183_m1-FAM), Ccl3 (Mm00441259_g1_FAM-MGB), Ccl2 (Mm00441242_m1_FAM-
190 MGB), Il1b (Mm00434228_m1_FAM-MGB), Anxa1 (Mm00440225_m1_FAM-MGB), Lgals3
191 (Mm00802901_m1_FAM-MGB), Stab2 (Mm00454684_m1_FAM-MGB), Arg1
192 (Mm00475988_m1_FAM-MGB), Il7r (Mm00434295_m1_FAM-MGB), Adam8
193 (Mm01163449_g1_FAM-MGB), Trem2 (Mm04209424_g1_FAM-MGB), Fpr2
194 (Mm00484464_s1_FAM-MGB), Spp1 (Mm00436767_m1_FAM-MGB), Fn1
195 (Mm01256744_m1_FAM-MGB), Col1a1 (Mm00801666_g1_FAM-MGB), Itgax
196 (Mm00498701_m1_FAM-MGB), Mmp12 (Mm00500554_m1_FAM-MGB), and Timp1
197 (Mm01341361_m1_FAM-MGB). Gene expression for all mRNA targets was normalized to
198 internal Hprt mRNA transcript levels using Hrpt Taqman assay (Mm03024075_m1_VIC-MGB).
199

200 **Pro-resolution preclinical drug trial.** D2-*mdx* mice (18-19 days-old, n=6, males and females)
201 were treated daily with pro-resolving, FPR2 agonist BMS-986235 (6mg/kg, oral gavage; HY-
202 131180, MedChemExpress) for 3 weeks. Control D2-*mdx* mice were administered saline (18–
203 19-day-old, n=6, males and females) for 3 weeks. BMS-986235 was initially resuspended in
204 10% DMSO (Sigma) and 90% corn oil (Sigma), and further diluted in cherry syrup (NDC-0395-
205 2662-16, Humco) for oral gavage. After treatment, hearts were harvested, imaged, flash-frozen
206 in liquid nitrogen-chilled isopentane and stored at –80°C for molecular and histopathological
207 analyses.
208
209 **Microscopy.** We used Olympus VS120-S5 Virtual Slide Scanning System with UPlanSApo
210 40×/0.95 objective, Olympus XM10 monochrome camera, and Olympus VS-ASW FL 2.7
211 imaging software. Analysis was performed using Olympus CellSens 1.13 and ImageJ FIJI
212 Version 2.1./1.53c software (National Institutes of Health). Brightfield whole tissue imaging was
213 performed using Labomed Luxeo 6Z Digital HD Stereo Microscope with 10x/22mm objective
214 and camera system.
215
216 **Statistics.** GraphPad Prism 9.2.0 was used for all statistical analyses of data. Statistical
217 analysis was performed using non-parametric Mann-Whitney tests. Data normality was
218 assessed for all statistical comparisons. All p-values less than 0.05 were considered statistically
219 significant; *$p < 0.05$, **$p < 0.01$, ***$p < 0.001$, and ****$p < 0.0001$. Data plots reported as scatter
220 plot with mean ± SD.
221
222 **Results**
223 ***D2-mdx model Exhibits Pediatric-Onset Cardiac Damage.***
224 We have previously described the use of D2-*mdx* model of DMD to define mechanisms
225 contributing to pediatric-onset severe skeletal muscle degeneration [41, 42]. Here we observed

226 extensive pericardial damage of the ventricular wall in juvenile (<6-week-old) D2-*mdx* hearts
227 (**Fig. 1A**). In contrast, the age-matched milder DMD model, B10-*mdx*, did not demonstrate any
228 conspicuous histopathology (**Fig. 1B**). In D2-*mdx,* the histopathological damage extended to
229 both the right and the left ventricular walls (**Fig. 1C**). Use of Sirius Red staining revealed
230 extensive fibrosis, which manifests at notable levels in both the endomysium and perimysium of
231 the ventricular walls in D2-*mdx* (**Fig. 1D**). Whole tissue cross-sectional analysis of H&E and
232 Sirius Red stained hearts revealed increased cardiac wall damage and cardiomyocyte
233 degeneration ($p<0.001$) (**Fig. 1C, E, F**), and a concomitant increase in fibrosis ($p<0.05$) in the
234 juvenile D2-*mdx* hearts compared to age-matched B10-*mdx* hearts (**Fig. 1D, G, H**). The extent
235 of damage in D2-*mdx* mice varied between the mice, reaching up to nearly 20% of total cardiac
236 muscle cross-sectional area in the most affected case (**Fig. 1E, F**). Reminiscent of the skeletal
237 muscle damage in D2-*mdx*, the cardiac muscle also exhibited increased calcification in
238 damaged areas, which was exclusive to juvenile D2-*mdx* hearts (**Supplemental Fig. 1**). With
239 mixed reports of cardiac pathology in older DBA2/J wildtype (D2-WT) hearts[43, 44], we assessed if
240 the juvenile-onset cardiac damage was also a feature of the juvenile D2-WT mice. Hearts from
241 juvenile D2-WT showed no signs of gross pathology and were comparable to the hearts from
242 the age-matched B10 wildtype (B10-WT) mice (**Supplemental Fig. 2A, B**). This was further
243 confirmed by the microscopic evaluation that showed absence of any endomysial or perimysial
244 fibrosis or calcification in the D2-WT hearts throughout the left and right ventricular walls
245 (**Supplemental Fig. 2C, D**). Overall, these histopathological analyses reveal early onset
246 spontaneous cardiac damage with significant fibro-calcification in the D2-*mdx*, offering a model
247 to investigate the mechanisms of pediatric-onset cardiac damage and accompanying
248 endomysial fibrosis observed in DMD.
249
250 **Dysregulated inflammatory response characterize cardiac damage in juvenile D2-*mdx***

251 To identify the molecular alterations associated with the pediatric- versus adult-onset
252 cardiac damage caused by dystrophin deficit, we performed a comparative transcriptomic
253 analysis of hearts from D2-*mdx* and B10-*mdx* mice. Using bulk RNA sequencing we examined
254 genes that are differentially expressed (Log_2FC 0.6 and p_{adj} value 0.05) between the 6-week-old
255 male B10-*mdx* and D2-*mdx* hearts. This identified a total of 5,344 differentially expressed genes
256 (DEGs) representing 22.3% of all protein-coding murine genes. Principal component analysis
257 (PCA) identified that gene expression profiles of D2-*mdx* hearts were distinctly segregated from
258 B10-*mdx* along both PC1 (72% variance) and PC2 (15% variance) axes (**Fig. 2A**). Intra- and
259 inter sample variability of DEGs by heatmap analysis of the top 2,719 DEGs revealed consistent
260 trends for both up- and down-regulated genes based on the genotype at disease onset, with
261 1,586 genes upregulated in D2-*mdx* and 1,133 genes upregulated in B10-*mdx* (**Fig. 2B**).
262 To identify the functions of the DEGs and assess how they may contribute to the observed
263 histopathology and functional deficit in juvenile D2-*mdx* hearts, we performed Gene Set
264 Enrichment Analysis (GSEA) using our DESeq2 pairwise comparison results (0.6 log_2FC and
265 0.05 adjusted p-value), followed by gene ontology (GO) analysis using Cytoscape's
266 EnrichmentMap pipeline (**Fig. 2C**). GO EnrichmentMap analysis predominantly indicated that
267 upregulated DEGs in the juvenile D2-*mdx* fell within biological processes (BP) specific to
268 immune response and extracellular matrix organization and remodeling. These included GOBP
269 terms implicated in regulation of the inflammatory response, immune cell activation, leukocyte
270 chemotaxis and migration, and cytokine signaling (**Fig. 2C,** red clusters), as well as extracellular
271 matrix organization and disassembly, osteoblast differentiation, substrate adhesion and bone
272 remodeling, and overall tissue homeostasis (**Fig. 2C,** blue clusters). Outputs from GSEA
273 provided a comprehensive GO analysis of all upregulated and downregulated GOBP terms,
274 their respective normalized enrichment scores (NES), p-values, and enrichment plots identifying
275 alterations in inflammatory and extracellular matrix GOBPs have strongest positive enrichment
276 scores (ES) (**Supplemental Table 1**, **Supplemental Fig. 3**). The top 20 upregulated GOBP

277 terms identified dysregulation of the inflammatory response or extracellular matrix architecture
278 that included a total of 331 upregulated DEGs common between them (**Supplemental Table 2**).
279 This was validated by the quantification of the normalized expression for the top 20 most
280 upregulated DEGs specific to unique GOBPs such as inflammatory response (GO:0006954)
281 (**Fig. 2D**) and external encapsulating structure (extracellular matrix) organization (GO:0045229)
282 (**Fig. 2E**). The leading-edge genes identified increased expression of pro-inflammatory
283 chemokines, and components of fibrotic extracellular matrix remodeling as potential drivers of
284 overt pediatric-onset cardiac damage in the D2-*mdx* (**Figure 2, Supplementary Fig. 3**).
285 To independently validate the role of aberrant acute inflammatory response of granulocyte
286 and leukocyte chemotaxis by way of chemokine/cytokine signaling pathways, we examined
287 these genes by qPCR in an expanded (n = 9 D2-*mdx* and n = 7 B10-*mdx*) cohort of juvenile
288 *mdx* mice. This validated our findings from RNAseq analysis and confirmed significant
289 upregulation of macrophage-secreted pro-inflammatory C-C family chemokines, *Ccl3*
290 (macrophage inflammatory protein-1α) and *Ccl8* (monocyte chemoattractant protein-2), that
291 regulate neutrophil, monocyte and lymphocyte chemotaxis following acute tissue damage (**Fig.
292 3A**; $p<0.001$). Similarly, expression of *Il7r* (interleukin-7 receptor), that promotes neutrophil and
293 monocyte recruitment, was also found upregulated in D2-*mdx* hearts (**Fig. 3A**; $p<0.001$), while,
294 expression of *Stab2* (stabilin-2), a macrophage-expressed phosphatidylserine (PS) surface
295 receptor that mediates phagocytosis and extracellular matrix remodeling during inflammation [45],
296 was also upregulated in D2-*mdx* hearts (**Fig. 3A**; $p<0.001$). Expression of *Adam8* (a disintegrin
297 and metalloproteinase 8), that promotes release of pro-inflammatory cytokines and cell
298 adhesion molecules and degradation of extracellular matrix [46], was also highly overexpressed in
299 D2-*mdx* hearts in accordance with bulk RNAseq results (**Fig. 3A**; $p<0.001$). *Trem2* (triggering
300 receptor expressed on myeloid cells 2), which drives NF-kB signaling and production of pro-

301 inflammatory cytokines including IL-6 and TNFα [47], was also upregulated in juvenile D2-*mdx*
302 hearts (**Fig. 3A**; *p<0.01*).
303 With the abundant increase in inflammatory cell chemokines, we examined the abundance
304 of macrophages using the pan-macrophage marker F4/80. This confirmed extensive presence
305 of macrophages in the damaged regions in D2-*mdx* hearts, which is distinct from what is
306 observed in the B10-*mdx* hearts (**Fig. 3C, D;** *top panels*). To assess the attributes of infiltrating
307 macrophages in the D2-*mdx* hearts, we next profiled transcript levels of *Il-1b* (interleukin-1b), a
308 pro-inflammatory macrophage marker, *Arg1* (arginase-1), a pro-regenerative macrophage
309 marker, and *Lgals3* (galectin-3), a pathogenic macrophage marker[48, 49]. While the inflammatory
310 and regenerative marker genes were increased by 3-, and 9-folds respectively in D2-*mdx*,
311 compared to B10-*mdx* hearts, the levels of pathogenic marker (*Lgals3*) was elevated by ~45-
312 fold (*p<0.001*) (**Fig. 3B**). To determine if the different genetic background may contribute to this
313 dysregulation we examined these transcripts in age-matched juvenile D2-WT and B10-WT
314 mice. This showed no influence of genetic background for *Adam8*, *Il1b*, *Lgals3*, and *Arg1*
315 between strains, and minimal impact on the expression of *Ccl3* (*p<0.01*), *Ccl8* (*p<0.01*), *Trem2*
316 (*p<0.01*), and *Il7r* (*p<0.05*) (**Supplemental Fig. 4A**). As our previous investigations have
317 revealed galectin-3 enriched macrophages as a driver of fibrotic degeneration of D2-*mdx*
318 skeletal muscles[50], we assessed the tissue localization and abundance galectin-3 protein (GAL-
319 3) in D2-*mdx*. This identified that GAL-3$^+$ macrophages were highly abundant and nearly
320 exclusively localized within the damaged regions of D2-*mdx* hearts (**Fig. 3C**), while in
321 accordance with qPCR results, these pathogenic macrophages were absent in B10-*mdx* hearts
322 (**Fig. 3B**, **D**).
323 Increased expression of chemokines observed in these tissues explains the excess of
324 macrophages in D2-*mdx*. However, during acute injury, the inflammatory response is controlled
325 by a pro-resolving response that follows cytokine-mediated activation of inflammation and
326 involves activation of the G protein coupled receptors including Formyl peptide receptors

327 (FPRs). FPRs are activated by the endogenous ligands produced in response to tissue damage,
328 including lipids (Resolvin D1, Lipoxin A4) and protein (Annexin A1; AnxA1) that bind FPR1/2[51,
329 52, 53] and serve as the master switch at the site of damage that helps resolve the inflammation.
330 They do so by promoting macrophage skewing from pro- to anti-inflammatory fates and
331 regulating signaling pathways that help clear immune cell infiltration by activating their apoptosis
332 and non-phlogistic clearance as well [53, 54, 55, 56, 57]. To assess if the excessive inflammatory
333 responses in D2-*mdx* hearts is due to reduced FPR signaling, we examined the expression of
334 FPRs (*Fpr1*, *Fpr2*) and its ligand *Anxa1*. This revealed over 4-fold upregulation of FPRs (both
335 *Fpr1* and *Fpr2*) expression in D2-*mdx* relative to B10-*mdx* heart, but no change in the
336 expression of *Anxa1* between D2-*mdx* and B10-*mdx* (**Fig. 3B**). These results validated the
337 findings from the previous cohort used for bulk RNAseq analysis (**Fig. 2, Supplementary Table**
338 **1**). Together, they suggest reduced activation of FPR signaling hinders resolution of
339 inflammation and may be a driver of the excessive inflammation seen in juvenile D2-*mdx* hearts,
340 which in turn is linked to their fibro-degenerative state.
341
342 **Fibrotic ECM remodeling drives early onset cardiac fibrosis in juvenile D2-*mdx*.**
343 To evaluate the prominent upregulation of ECM remodeling pathways implicated by the
344 RNAseq analysis, we performed qPCR for multiple extracellular matrix-associated components
345 and remodeling enzymes identified by the analysis of our bulk RNAseq cohort. This validated
346 the observed upregulation of *Fn1 (*fibronectin; *p<0.01), Col1a1 (*collagen 1A; *p=0.0712), and*
347 *Itgax* (integrin alpha X; *p<0.001)* in D2-*mdx* hearts, relative to B10-*mdx* (**Fig. 4A**). Assessment
348 of *Spp1* (osteopontin), a DMD genetic modifier that links inflammation to extracellular matrix
349 assembly and fibrosis [58, 59, 60, 61, 62] and macrophage-expressed matrix remodeling enzyme
350 *Mmp12 (*matrix metalloproteinase 12), both showed over 200-fold upregulation in D2-*mdx*
351 hearts, compared to B10-*mdx* (**Fig. 4A**). While other ECM regulator and structural components
352 including *Timp1 (*TIMP metallopeptidase inhibitor 1), *Itgax*, *Fn1*, and *Col1a1* showed between 4-

353 40-fold upregulation in D2-*mdx* hearts (**Fig. 4A**). These validate the findings from the bulk
354 RNAseq cohort and implicate a nexus of inflammatory-ECM dysregulation in pediatric-onset
355 cardiac pathogenesis in the D2-*mdx*. To monitor the sites of fibrosis in juvenile D2-*mdx* hearts,
356 we immunostained heart cross-sections for COL1A1 and co-stained with wheat germ agglutinin
357 (WGA), which showed dense COL1A1 expression in D2-*mdx* in the damaged regions along the
358 RV wall and throughout the endomysium (**Fig. 4B, B'**), while endomysial COL1A1 staining in
359 B10-*mdx* counterparts was minimal in comparison (**Fig. 4C, C'**). To address the influence of
360 genetic background on the above findings, we assessed expression in D2-WT and B10-WT
361 hearts, which indicated no genotype-related differences in the expression of *Fn1*, *Col1a1*, *Itgax*,
362 or *Timp1*, and a comparatively modest increases in the expression of *Spp1* ($p<0.01$) and
363 *Mmp12* ($p<0.01$) in D2-WT hearts, relative to B10-WT (**Supplemental Fig. 4B**), when compared
364 to differences between mdx strains (**Fig. 4A**). This identified the site and composition of the
365 fibrotic ECM in the D2-*mdx* heart. It also highlighted the potential of targeting the aberrant pro-
366 inflammatory response to attenuate fibrotic cardiac degeneration of the D2-*mdx* dystrophic
367 heart.
368
369 **Activation of pro-resolving FPR signaling prevents cardiac damage in D2-*mdx* hearts.**
370 The above findings link inflammation and cardiac fibrosis in D2-*mdx*. With mixed success of
371 corticosteroid use in treating this in heart by dampening inflammation, coupled with our findings
372 of poor activation of pro-resolving FPR signaling, we hypothesized use of FPR-targeting therapy
373 may resolve the chronic inflammation, without blocking acute inflammation required for the
374 reparative ability of the injured tissue[63, 64] (**Fig. 5A**).
375 To assess the benefit of a pro-resolving FPR-agonist therapy for pediatric-onset cardiac
376 pathology in D2-*mdx*, we tested use of the synthetic FPR agonist BMS-986235 versus saline (n
377 = 6 animals/cohort). Mice were orally dosed with drug beginning at 2.5-weeks of age (just prior
378 to the onset of cardiac pathology) and were maintained on drug (or saline) till 6-weeks of age

379 when tissues were harvested for further analysis (**Fig. 5B**). Analysis of histopathology of the
380 cardiac tissue cross-section revealed a clear lack of fibro-calcified damaged areas along the RV
381 and LV walls in drug-treated hearts, compared to saline controls (**Fig. 5C**). Histological analyses
382 performed by H&E staining, confirmed this observed therapeutic effect with some of the drug-
383 treated hearts showing only small and discrete areas of damage within the RV wall, and the rest
384 lacked any signs of damage or inflammation altogether, while the saline-treated mice showed
385 extensive cardiac damage (**Fig. 5D**). To further assess this impact of pro-resolving therapy on
386 inflammation and extracellular matrix remodeling in D2-*mdx* hearts, we immunostained tissue
387 cross-sections for macrophages, which confirmed the reduction in macrophage infiltration
388 through the heart and within and surrounding any small sites of damage that existed in our
389 treated cohort (**Fig. 5E**). This was in stark contrast to the heightened macrophage infiltration
390 both within and surrounding sites of damage in saline control hearts (**Fig. 5E**). Next, to more
391 directly assess fibrotic gene expression we immunostained these hearts for COL1A1 and found
392 the drug treatment also significantly reduced the COL1A1 expression throughout the heart,
393 when compared to the expression in the saline controls (**Fig. 5F**).
394 To assess the effect of acute BMS-986235 treatment on inflammation and extracellular
395 matrix remodeling pathways, we next performed targeted qPCR for both inflammatory- and
396 extracellular matrix remodeling-associated transcripts previously shown to be dysregulated in
397 D2-*mdx* hearts (**Fig. 2-4**). We found acute BMS-986235 treatment of juvenile D2-*mdx* mice
398 resulted in a significant reduction in the levels of inflammatory transcripts *Trem2*, *Lgals3*, and
399 *Anxa1* (**Fig. 5G**), confirming the efficacy of this pro-resolving therapy to attenuate aberrant
400 inflammatory signaling via the FPR2-ANXA1 axis. Similarly, quantification of extracellular matrix
401 remodeling targets, *Spp1*, *Timp1,* and *Col1a1*, showed significant depletion of *Spp1* and *Timp1*
402 transcripts (**Fig. 5H**), and a trending reduction in *Col1a1* transcript levels (**Fig. 5H**) which aligns
403 with COL1A1 immunostaining results (**Fig. 5F**). Future chronic studies will be required to assess

404 the full benefit of chronic pro-resolving therapy to delay the onset and lessen the severity of
405 fibrotic cardiac degeneration with disease progression in older D2-*mdx* mice.
406
407 **Discussion**
408 While there has been a long-standing recognition of early-onset cardiac deficit and its lethal
409 consequences for boys with DMD, our experimental understanding of the molecular deficits and
410 preclinical interventions have been based on the use of adult mouse models. This is due to the
411 late onset of cardiac damage in the *mdx* mouse model. Our studies here introduce D2-*mdx* as a
412 model that manifests pediatric-onset cardiac damage. Histopathological analyses reveal early
413 onset spontaneous cardiac damage with significant fibro-calcification in the D2-*mdx* model,
414 offering an opportunity to investigate the mechanisms of pediatric-onset cardiac damage and
415 accompanying endomysial fibrosis observed in DMD.
416 Our studies here identify dysregulation of inflammatory and ECM remodeling as two such
417 pathological pathways. Next, we focused on harnessing underlying molecular pathways that
418 distinguish the cardiac deficit in D2-*mdx* model as compared to the adult-onset cardiac deficit
419 B10-*mdx* model. This analysis allowed distinguishing the differences driving the onset of mild
420 and severe cardiac muscle degeneration and cardiomyopathy independent of the
421 presence/absence of dystrophin protein. Such differences are reminiscent of the DMD patients,
422 who manifest varying level and severity of cardiomyopathy despite the lacking dystrophin
423 expression.
424 Our studies identify excessive inflammatory response that fails to resolve through FPR2-
425 mediated pro-resolving pathway prevents restoring the injured heart tissues to their uninflamed
426 state. While the infiltrating leukocytes are needed in damaged heart to clear the dead cells,
427 FPR2 and other mediators that repress inflammation are released leading to predominance of
428 anti-inflammatory cells - a response associated with activation of cardiac repair. We find that
429 this latter repressive response is poor, and that the excessive inflammatory signaling proceeds

430 via Spp1 and TGFβ pathway to activate downstream cardiac fibrosis and other degenerative
431 response. Activation of these profibrotic degenerative response have long been recognized as
432 a feature of the D2-*mdx* model[65] which we previously showed contributes to excessive skeletal
433 muscle pathology in the juvenile D2-*mdx* mice by suppression of skeletal muscle regeneration[41,
434 42]. Unlike skeletal muscle, cardiac muscle does not undergo regeneration and our comparative
435 analysis of D2-*mdx* and B10-*mdx* identify cardiomyocyte degeneration due to chronic
436 inflammation and loss by way of fibro-calcified ECM. We observe the ventricular pericardium as
437 the region most affected by this damage, but this can progress to the atria as well (**Fig. 1**). This
438 variability in the affected region is in addition to the variability we observe in the severity of
439 cardiac damage between individual mice. This hints at a level of stochasticity in the
440 degeneration. We believe this may plausibly reflect the level of initial damage to the affected
441 heart, which is then amplified as the inflammation ensues becoming chronic.
442 We find chronic cardiac inflammation in D2-*mdx* is marked by higher level of activation of
443 inflammatory and immune response in part by higher expression of chemokines that attract
444 these immune cells (**Fig. 2, 3**). This inflammatory response involves accumulation of
445 *Spp1*(OPN)/*Lgals3*(GAL-3) expressing pathogenic macrophages that we recently identified by
446 single cell RNAseq analysis of the skeletal muscles from *mdx* mice[49]. Osteopontin secreted by
447 these macrophages promote skeletal muscle fibrosis by activating the stromal progenitors and
448 we suggest a similar mechanism may be in place following accumulation of these macrophage
449 in the damaged heart (**Fig. 3**). In support of this mechanism, we find these GAL-3^{+}
450 macrophages enriched in the same pericardial region that are enriched in COLA1 indicative of
451 active fibrosis (**Fig. 3**). The indication that this is an active phenomenon comes from the
452 concomitant enrichment of other ECM building (fibronectin) and degrading (TIMP/MMP)
453 components along with leukocyte attracting (CCCL3/8) and resolution (FPR1/2) signaling (**Fig.
454 2-4**). This dynamic indicated that there is a likely shift in the equilibrium of these two opposing -
455 inflammation building and resolving signals, and hence rebalancing this could provide a likely

456 beneficial effect for the affected region. This is in line with the fact that while acute inflammation
457 following tissue damage is essential for cardiac repair, chronic inflammation can be disruptive[66].
458 To address this ensuing imbalance of these two opposing inflammatory signaling we made use
459 of the pro-resolving therapy that unlike GCs, precisely targets the resolution of inflammation by
460 activating FPR2 signaling, but not blocking activation of inflammation by NFkb or related pro-
461 inflammatory pathways. This approach showed excellent promise such that a short (3 week)
462 treatment of juvenile D2-*mdx* mice allowed full resolution of inflammation and prevented any
463 subsequent fibrotic cardiac damage detected histologically as well as by way of aberrant
464 molecular signature including *Gal3*/*Spp1* macrophages and *Col1A1* and *Fn1* expressing stromal
465 cells (**Fig. 5**).
466 In summary, our studies introduce the D2-*mdx* as a model that manifests pediatric-onset
467 cardiac damage, which provides opportunities to investigate the drivers of early-onset
468 cardiomyopathy in DMD patients. We identified dysregulation of inflammatory and ECM
469 remodeling pathways as key contributors. Specifically, our findings highlight excessive and
470 unresolved inflammatory response involving pathogenic macrophages and neutrophils,
471 contributes to chronic inflammation and progressive cardiomyocyte degeneration and fibrotic
472 replacement in the D2-*mdx* model. Finally, our use of FPR2-targeting therapy provides a
473 potential therapeutic avenue to prevent or mitigate pediatric-onset cardiac pathologies in DMD.
474
475 **Author Contributions.** This study was conceived, and the experiments designed by JSN and
476 JKJ with inputs from all authors. RNAseq sample processing was conducted by JSN, RH, DAM,
477 and KP; bioinformatic analyses were performed by AL, PU, SB, ST, and VB. AL conducted
478 molecular analyses with help from YJM and ST. Histopathological analyses were conducted by
479 AL, RH, YJM, IHG, and GW. The manuscript was written by JSN, AL, and JKJ, and edited by all
480 authors. JKJ and JSN obtained funding and provided oversight for pursuit of the study.
481

Acknowledgements. This work was supported by funds provided by Children's National Research Institute (JSN) and the Foundation to Eradicate Duchenne (JKJ; JSN). JKJ and JSN acknowledge support from the Department of Defense DMDRP (W81XWH2110711| JSN; W81XWH2110680 | JKJ) for their work on DMD. Microscopy was performed at the Cell and Tissue Microscopy Core supported by CNRI and The National Institutes of Health NICHD (P50HD105328 | JKJ).

Competing interests. JKJ and JSN have filed a provisional intellectual property application related to the findings reported in this manuscript. The authors have no other active or potential competing or financial interests to declare.

492 **References.**

493 1. Duan D, Goemans N, Takeda S, Mercuri E, Aartsma-Rus A. Duchenne muscular dystrophy.
494 *Nat Rev Dis Primers* 2021, **7**(1)**:** 13.
495
496 2. Hoffman EP, Brown RH, Jr., Kunkel LM. Dystrophin: the protein product of the Duchenne
497 muscular dystrophy locus. *Cell* 1987, **51**(6)**:** 919-928.
498
499 3. Koenig M, Hoffman EP, Bertelson CJ, Monaco AP, Feener C, Kunkel LM. Complete cloning
500 of the Duchenne muscular dystrophy (DMD) cDNA and preliminary genomic organization of
501 the DMD gene in normal and affected individuals. *Cell* 1987, **50**(3)**:** 509-517.
502
503 4. Haslett JN, Sanoudou D, Kho AT, Bennett RR, Greenberg SA, Kohane IS*, et al.* Gene
504 expression comparison of biopsies from Duchenne muscular dystrophy (DMD) and normal
505 skeletal muscle. *Proc Natl Acad Sci U S A* 2002, **99**(23)**:** 15000-15005.
506
507 5. Meyers TA, Townsend D. Cardiac Pathophysiology and the Future of Cardiac Therapies in
508 Duchenne Muscular Dystrophy. *Int J Mol Sci* 2019, **20**(17).
509
510 6. Serrano AL, Munoz-Canoves P. Fibrosis development in early-onset muscular dystrophies:
511 Mechanisms and translational implications. *Semin Cell Dev Biol* 2017, **64:** 181-190.
512
513 7. Shin J, Tajrishi MM, Ogura Y, Kumar A. Wasting mechanisms in muscular dystrophy. *Int J*
514 *Biochem Cell Biol* 2013, **45**(10)**:** 2266-2279.
515
516 8. Mavrogeni S, Markousis-Mavrogenis G, Papavasiliou A, Kolovou G. Cardiac involvement in
517 Duchenne and Becker muscular dystrophy. *World J Cardiol* 2015, **7**(7)**:** 410-414.

9. Melacini P, Fanin M, Danieli GA, Villanova C, Martinello F, Miorin M*, et al.* Myocardial involvement is very frequent among patients affected with subclinical Becker's muscular dystrophy. *Circulation* 1996, **94**(12)**:** 3168-3175.

10. Solheim TA, Fornander F, Raja AA, Mogelvang R, Poulsen NS, Duno M*, et al.* Cardiac Involvement in Women With Pathogenic Dystrophin Gene Variants. *Front Neurol* 2021, **12:** 707838.

11. Finsterer J, Stollberger C. The heart in human dystrophinopathies. *Cardiology* 2003, **99**(1)**:** 1-19.

12. Van Erp C, Loch D, Laws N, Trebbin A, Hoey AJ. Timeline of cardiac dystrophy in 3-18-month-old MDX mice. *Muscle Nerve* 2010, **42**(4)**:** 504-513.

13. Li W, Liu W, Zhong J, Yu X. Early manifestation of alteration in cardiac function in dystrophin deficient mdx mouse using 3D CMR tagging. *J Cardiovasc Magn Reson* 2009, **11**(1)**:** 40.

14. Gordish-Dressman H, Willmann R, Dalle Pazze L, Kreibich A, van Putten M, Heydemann A*, et al.* "Of Mice and Measures": A Project to Improve How We Advance Duchenne Muscular Dystrophy Therapies to the Clinic. *J Neuromuscul Dis* 2018, **5**(4)**:** 407-417.

542 15. Grady RM, Teng H, Nichol MC, Cunningham JC, Wilkinson RS, Sanes JR. Skeletal and
543 cardiac myopathies in mice lacking utrophin and dystrophin: a model for Duchenne muscular
544 dystrophy. *Cell* 1997, **90**(4)**:** 729-738.
545
546 16. Aartsma-Rus A, van Putten M, Mantuano P, De Luca A. On the use of D2.B10-
547 Dmdmdx/J (D2.mdx) Versus C57BL/10ScSn-Dmdmdx/J (mdx) Mouse Models for Preclinical
548 Studies on Duchenne Muscular Dystrophy: A Cautionary Note from Members of the TREAT-
549 NMD Advisory Committee on Therapeutics. *J Neuromuscul Dis* 2023, **10**(1)**:** 155-158.
550
551 17. De Giorgio D, Novelli D, Motta F, Cerrato M, Olivari D, Salama A*, et al.* Characterization
552 of the Cardiac Structure and Function of Conscious D2.B10-Dmd(mdx)/J (D2-mdx) mice from
553 16-17 to 24-25 Weeks of Age. *Int J Mol Sci* 2023, **24**(14).
554
555 18. Heydemann A, Ceco E, Lim JE, Hadhazy M, Ryder P, Moran JL*, et al.* Latent TGF-beta-
556 binding protein 4 modifies muscular dystrophy in mice. *J Clin Invest* 2009, **119**(12)**:** 3703-
557 3712.
558
559 19. Flanigan KM, Ceco E, Lamar KM, Kaminoh Y, Dunn DM, Mendell JR*, et al.* LTBP4
560 genotype predicts age of ambulatory loss in Duchenne muscular dystrophy. *Ann Neurol*
561 2013, **73**(4)**:** 481-488.
562
563 20. Tandon A, Villa CR, Hor KN, Jefferies JL, Gao Z, Towbin JA*, et al.* Myocardial fibrosis
564 burden predicts left ventricular ejection fraction and is associated with age and steroid
565 treatment duration in duchenne muscular dystrophy. *J Am Heart Assoc* 2015, **4**(4).
566

567 21. Schram G, Fournier A, Leduc H, Dahdah N, Therien J, Vanasse M*, et al.* All-cause
568 mortality and cardiovascular outcomes with prophylactic steroid therapy in Duchenne
569 muscular dystrophy. *J Am Coll Cardiol* 2013, **61**(9)**:** 948-954.
570
571 22. Bourke J, Turner C, Bradlow W, Chikermane A, Coats C, Fenton M*, et al.* Cardiac care
572 of children with dystrophinopathy and females carrying DMD-gene variations. *Open Heart*
573 2022, **9**(2).
574
575 23. Janssen PM, Murray JD, Schill KE, Rastogi N, Schultz EJ, Tran T*, et al.* Prednisolone
576 attenuates improvement of cardiac and skeletal contractile function and histopathology by
577 lisinopril and spironolactone in the mdx mouse model of Duchenne muscular dystrophy.
578 *PLoS One* 2014, **9**(2)**:** e88360.
579
580 24. Heier CR, Yu Q, Fiorillo AA, Tully CB, Tucker A, Mazala DA*, et al.* Vamorolone targets
581 dual nuclear receptors to treat inflammation and dystrophic cardiomyopathy. *Life Sci Alliance*
582 2019, **2**(1).
583
584 25. Mavrogeni S, Giannakopoulou A, Papavasiliou A, Markousis-Mavrogenis G, Pons R,
585 Karanasios E*, et al.* Cardiac profile of asymptomatic children with Becker and Duchenne
586 muscular dystrophy under treatment with steroids and with/without perindopril. *BMC*
587 *Cardiovasc Disord* 2017, **17**(1)**:** 197.
588
589 26. Guglieri M, Bushby K, McDermott MP, Hart KA, Tawil R, Martens WB*, et al.* Effect of
590 Different Corticosteroid Dosing Regimens on Clinical Outcomes in Boys With Duchenne
591 Muscular Dystrophy: A Randomized Clinical Trial. *JAMA* 2022, **327**(15)**:** 1456-1468.
592

27. Butterfield RJ, Kirkov S, Conway KM, Johnson N, Matthews D, Phan H*, et al.* Evaluation of effects of continued corticosteroid treatment on cardiac and pulmonary function in non-ambulatory males with Duchenne muscular dystrophy from MD STARnet. *Muscle Nerve* 2022, **66**(1)**:** 15-23.

28. Sinniah A, Yazid S, Flower RJ. From NSAIDs to Glucocorticoids and Beyond. *Cells* 2021, **10**(12).

29. Gobbetti T, Cooray SN. Annexin A1 and resolution of inflammation: tissue repairing properties and signalling signature. *Biol Chem* 2016, **397**(10)**:** 981-993.

30. McArthur S, Juban G, Gobbetti T, Desgeorges T, Theret M, Gondin J*, et al.* Annexin A1 drives macrophage skewing to accelerate muscle regeneration through AMPK activation. *J Clin Invest* 2020, **130**(3)**:** 1156-1167.

31. Leikina E, Defour A, Melikov K, Van der Meulen JH, Nagaraju K, Bhuvanendran S*, et al.* Annexin A1 Deficiency does not Affect Myofiber Repair but Delays Regeneration of Injured Muscles. *Sci Rep* 2015, **5:** 18246.

32. D'Acquisto F, Perretti M, Flower RJ. Annexin-A1: a pivotal regulator of the innate and adaptive immune systems. *Br J Pharmacol* 2008, **155**(2)**:** 152-169.

33. Perretti M, Dalli J. Resolution Pharmacology: Focus on Pro-Resolving Annexin A1 and Lipid Mediators for Therapeutic Innovation in Inflammation. *Annu Rev Pharmacol Toxicol* 2023, **63:** 449-469.

619 34. Tourki B, Kain V, Pullen AB, Norris PC, Patel N, Arora P*, et al.* Lack of resolution sensor
620 drives age-related cardiometabolic and cardiorenal defects and impedes inflammation-
621 resolution in heart failure. *Mol Metab* 2020, **31:** 138-149.
622
623 35. Qin C, Buxton KD, Pepe S, Cao AH, Venardos K, Love JE*, et al.* Reperfusion-induced
624 myocardial dysfunction is prevented by endogenous annexin-A1 and its N-terminal-derived
625 peptide Ac-ANX-A1(2-26). *Br J Pharmacol* 2013, **168**(1)**:** 238-252.
626
627 36. Kain V, Ingle KA, Colas RA, Dalli J, Prabhu SD, Serhan CN*, et al.* Resolvin D1 activates
628 the inflammation resolving response at splenic and ventricular site following myocardial
629 infarction leading to improved ventricular function. *J Mol Cell Cardiol* 2015, **84:** 24-35.
630
631 37. Kain V, Liu F, Kozlovskaya V, Ingle KA, Bolisetty S, Agarwal A*, et al.* Resolution Agonist
632 15-epi-Lipoxin A(4) Programs Early Activation of Resolving Phase in Post-Myocardial
633 Infarction Healing. *Sci Rep* 2017, **7**(1)**:** 9999.
634
635 38. Garcia RA, Lupisella JA, Ito BR, Hsu MY, Fernando G, Carson NL*, et al.* Selective FPR2
636 Agonism Promotes a Proresolution Macrophage Phenotype and Improves Cardiac Structure-
637 Function Post Myocardial Infarction. *JACC Basic Transl Sci* 2021, **6**(8)**:** 676-689.
638
639 39. Lupisella J, St-Onge S, Carrier M, Cook EM, Wang T, Sum C*, et al.* Molecular
640 Mechanisms of Desensitization Underlying the Differential Effects of Formyl Peptide
641 Receptor 2 Agonists on Cardiac Structure-Function Post Myocardial Infarction. *ACS*
642 *Pharmacol Transl Sci* 2022, **5**(10)**:** 892-906.
643

644 40. Bulfield G, Siller WG, Wight PA, Moore KJ. X chromosome-linked muscular dystrophy
645 (mdx) in the mouse. *Proc Natl Acad Sci U S A* 1984, **81**(4)**:** 1189-1192.
646
647 41. Mazala DA, Novak JS, Hogarth MW, Nearing M, Adusumalli P, Tully CB*, et al.* TGF-
648 beta-driven muscle degeneration and failed regeneration underlie disease onset in a DMD
649 mouse model. *JCI Insight* 2020, **5**(6).
650
651 42. Mazala DAG, Hindupur R, Moon YJ, Shaikh F, Gamu IH, Alladi D*, et al.* Altered muscle
652 niche contributes to myogenic deficit in the D2-mdx model of severe DMD. *Cell Death Discov*
653 2023, **9**(1)**:** 224.
654
655 43. Hakim CH, Wasala NB, Pan X, Kodippili K, Yue Y, Zhang K*, et al.* A Five-Repeat Micro-
656 Dystrophin Gene Ameliorated Dystrophic Phenotype in the Severe DBA/2J-mdx Model of
657 Duchenne Muscular Dystrophy. *Mol Ther Methods Clin Dev* 2017, **6:** 216-230.
658
659 44. Hart CC, Lee YI, Hammers DW, Sweeney HL. Evaluation of the DBA/2J mouse as a
660 potential background strain for genetic models of cardiomyopathy. *J Mol Cell Cardiol Plus*
661 2022, **1**.
662
663 45. Kayashima Y, Clanton CA, Lewis AM, Sun X, Hiller S, Huynh P*, et al.* Reduction of
664 Stabilin-2 Contributes to a Protection Against Atherosclerosis. *Front Cardiovasc Med* 2022,
665 **9:** 818662.
666
667 46. Nishimura D, Sakai H, Sato T, Sato F, Nishimura S, Toyama-Sorimachi N*, et al.* Roles of
668 ADAM8 in elimination of injured muscle fibers prior to skeletal muscle regeneration. *Mech*
669 *Dev* 2015, **135:** 58-67.

670

671 47. Wang M, Gao X, Zhao K, Chen H, Xu M, Wang K. Effect of TREM2 on Release of
672 Inflammatory Factor from LPS-stimulated Microglia and Its Possible Mechanism. *Ann Clin*
673 *Lab Sci* 2019, **49**(2)**:** 249-256.
674

675 48. Villalta SA, Nguyen HX, Deng B, Gotoh T, Tidball JG. Shifts in macrophage phenotypes
676 and macrophage competition for arginine metabolism affect the severity of muscle pathology
677 in muscular dystrophy. *Human molecular genetics* 2009, **18**(3)**:** 482-496.
678

679 49. Coulis G, Jaime D, Guerrero-Juarez C, Kastenschmidt JM, Farahat PK, Nguyen Q*, et al.*
680 Single-cell and spatial transcriptomics identify a macrophage population associated with
681 skeletal muscle fibrosis. *bioRxiv* 2023.
682

683 50. Coulis G, Jaime D, Guerrero-Juarez C, Kastenschmidt JM, Farahat PK, Nguyen Q*, et al.*
684 Single-cell and spatial transcriptomics identify a macrophage population associated with
685 skeletal muscle fibrosis. *Sci Adv* 2023, **9**(27)**:** eadd9984.
686

687 51. Sanchez-Garcia S, Jaen RI, Fernandez-Velasco M, Delgado C, Bosca L, Prieto P.
688 Lipoxin-mediated signaling: ALX/FPR2 interaction and beyond. *Pharmacol Res* 2023, **197:**
689 106982.
690

691 52. Yang M, Song XQ, Han M, Liu H. The role of Resolvin D1 in liver diseases.
692 *Prostaglandins Other Lipid Mediat* 2022, **160:** 106634.
693

694 53. Perretti M, Godson C. Formyl peptide receptor type 2 agonists to kick-start resolution
695 pharmacology. *Br J Pharmacol* 2020, **177**(20)**:** 4595-4600.

696

697 54. Dahlgren C, Gabl M, Holdfeldt A, Winther M, Forsman H. Basic characteristics of the
698 neutrophil receptors that recognize formylated peptides, a danger-associated molecular
699 pattern generated by bacteria and mitochondria. *Biochem Pharmacol* 2016, **114:** 22-39.
700

701 55. Godson C, Mitchell S, Harvey K, Petasis NA, Hogg N, Brady HR. Cutting edge: lipoxins
702 rapidly stimulate nonphlogistic phagocytosis of apoptotic neutrophils by monocyte-derived
703 macrophages. *J Immunol* 2000, **164**(4)**:** 1663-1667.
704

705 56. Fredman G, Kamaly N, Spolitu S, Milton J, Ghorpade D, Chiasson R*, et al.* Targeted
706 nanoparticles containing the proresolving peptide Ac2-26 protect against advanced
707 atherosclerosis in hypercholesterolemic mice. *Sci Transl Med* 2015, **7**(275)**:** 275ra220.
708

709 57. Scannell M, Flanagan MB, deStefani A, Wynne KJ, Cagney G, Godson C*, et al.*
710 Annexin-1 and peptide derivatives are released by apoptotic cells and stimulate phagocytosis
711 of apoptotic neutrophils by macrophages. *J Immunol* 2007, **178**(7)**:** 4595-4605.
712

713 58. Vetrone SA, Montecino-Rodriguez E, Kudryashova E, Kramerova I, Hoffman EP, Liu SD*,*
714 *et al.* Osteopontin promotes fibrosis in dystrophic mouse muscle by modulating immune cell
715 subsets and intramuscular TGF-beta. *J Clin Invest* 2009, **119**(6)**:** 1583-1594.
716

717 59. Capote J, Kramerova I, Martinez L, Vetrone S, Barton ER, Sweeney HL*, et al.*
718 Osteopontin ablation ameliorates muscular dystrophy by shifting macrophages to a pro-
719 regenerative phenotype. *J Cell Biol* 2016, **213**(2)**:** 275-288.
720

721 60. Kramerova I, Kumagai-Cresse C, Ermolova N, Mokhonova E, Marinov M, Capote J*, et*
722 *al.* Spp1 (osteopontin) promotes TGFbeta processing in fibroblasts of dystrophin-deficient
723 muscles through matrix metalloproteinases. *Human molecular genetics* 2019, **28**(20)**:** 3431-
724 3442.
725
726 61. Hirata A, Masuda S, Tamura T, Kai K, Ojima K, Fukase A*, et al.* Expression profiling of
727 cytokines and related genes in regenerating skeletal muscle after cardiotoxin injection: a role
728 for osteopontin. *Am J Pathol* 2003, **163**(1)**:** 203-215.
729
730 62. Bello L, Pegoraro E. The "Usual Suspects": Genes for Inflammation, Fibrosis,
731 Regeneration, and Muscle Strength Modify Duchenne Muscular Dystrophy. *J Clin Med* 2019,
732 **8**(5).
733
734 63. Aurora AB, Porrello ER, Tan W, Mahmoud AI, Hill JA, Bassel-Duby R*, et al.*
735 Macrophages are required for neonatal heart regeneration. *J Clin Invest* 2014, **124**(3)**:** 1382-
736 1392.
737
738 64. Lavine KJ, Epelman S, Uchida K, Weber KJ, Nichols CG, Schilling JD*, et al.* Distinct
739 macrophage lineages contribute to disparate patterns of cardiac recovery and remodeling in
740 the neonatal and adult heart. *Proc Natl Acad Sci U S A* 2014, **111**(45)**:** 16029-16034.
741
742 65. Heydemann A, Ceco E, Lim JE, Hadhazy M, Ryder P, Moran JL*, et al.* Latent TGF-β–
743 binding protein 4 modifies muscular dystrophy in mice. *The Journal of clinical investigation*
744 2009, **119**(12)**:** 3703.
745

746 66. Frangogiannis NG. Regulation of the inflammatory response in cardiac repair. *Circ Res*
747 2012, **110**(1)**:** 159-173.
748
749
750

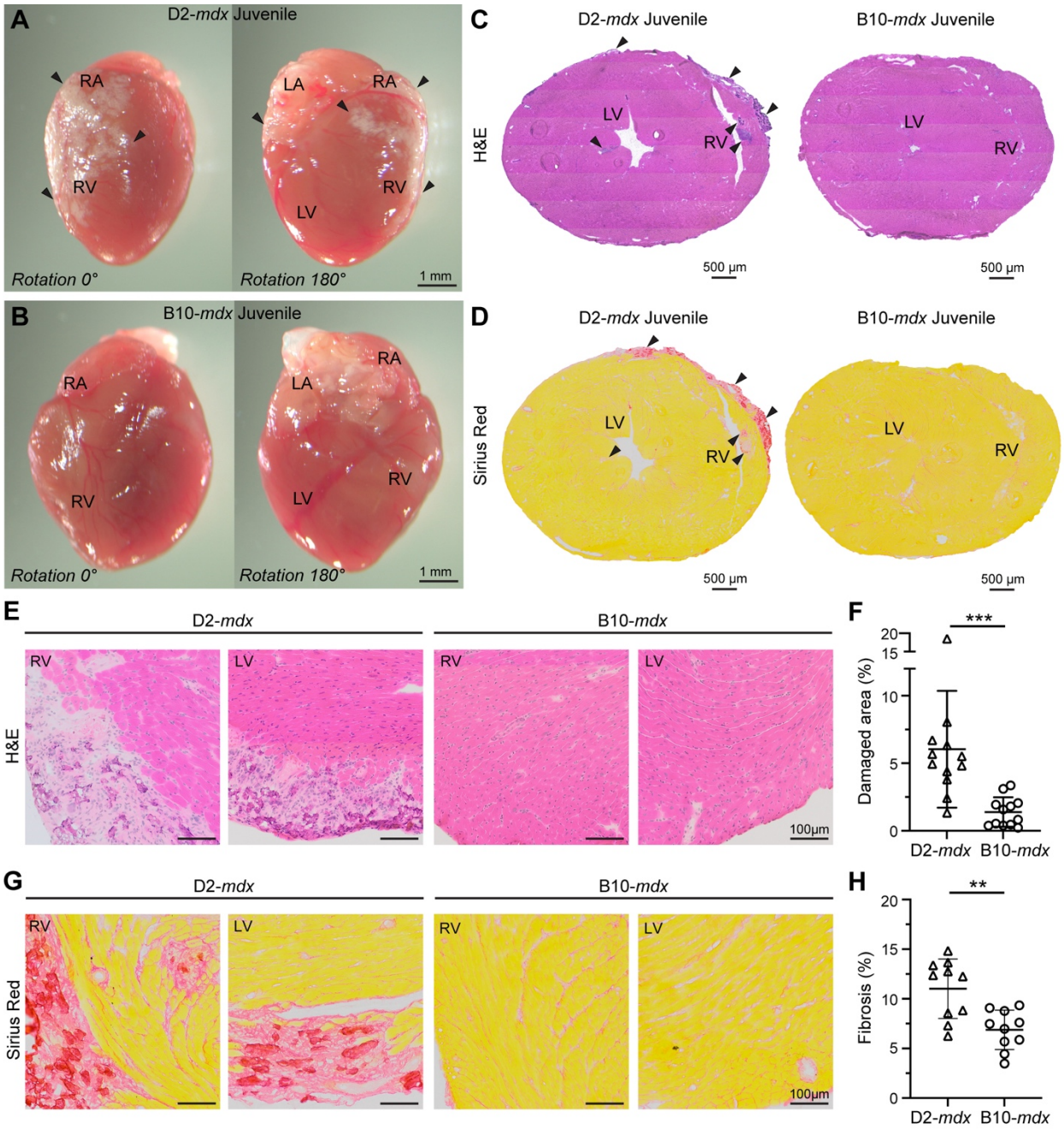

Figure 1. Histopathology associated with disease onset in juvenile D2-*mdx* hearts. Images show hearts harvested from juvenile (6 ± 0.5 wk) D2-*mdx* and B10-*mdx* mice at disease onset. **A-B.** Whole tissue images with matched orientation of D2-*mdx* (**A**) and B10-*mdx* (**B**) hearts showing ventricular and atrial fibro-calcified damage. **C-D.** Cross-sectional images of juvenile D2-*mdx* and B10-*mdx* hearts through the ventricular lumen, stained for histological features by H&E (**C**), and for fibrosis by Sirius Red (**D**). Arrowheads mark areas of fibrosis. **E-F.**

758 Image (**E**) and quantification (**F**) showing a portion of heart cross-section from juvenile D2-*mdx*
759 and B10-*mdx* hearts, showing damaged tissue areas characterized by the presence of
760 interstitial fibrosis, inflammatory cells and damaged cardiomyocytes. **G-H.** Image (**G**) and
761 quantification (**H**) showing a portion of heart cross-section from juvenile D2-*mdx* and B10-*mdx*
762 hearts labeled with Sirius Red to mark fibrotic tissue area in hearts from juvenile D2-*mdx* and
763 B10-*mdx* mice. Data represent mean ± SD from $n = 12$ hearts per cohort. Statistical analyses
764 performed using Mann Whitney U test; *$p < 0.05$, **$p < 0.001$, ***$p < 0.001$. Refer to
765 Supplementary Fig. 1-2 for additional details.
766
767

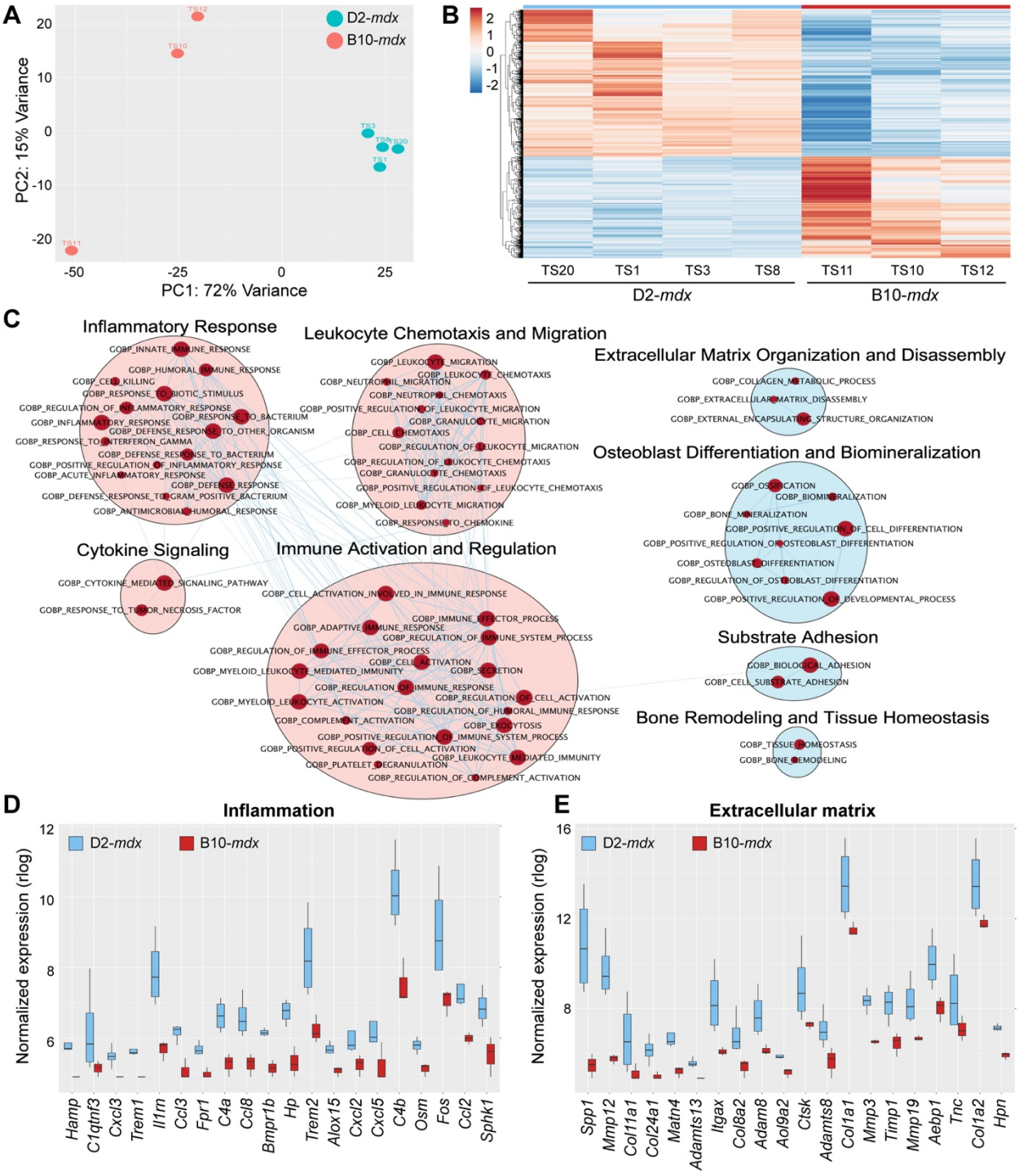

Figure 2. RNAseq analysis at disease onset in D2-*mdx* and age-matched B10-*mdx* hearts. Juvenile D2-*mdx* and B10-*mdx* hearts at disease onset (6 wk ± 0.5 wk) were analyzed by bulk tissue RNAseq. **A.** Dimensionality reduction of whole transcriptomic data via PCA (n=3-4 hearts/genotype) to assess sample clustering and inter-/intra-sample variance. **B.** Differential

773 gene expression analysis depicted via heatmap plot of 2,719 DEGs observed between D2-*mdx*
774 (blue) and B10-*mdx* (red), with 1,586 genes upregulated for D2-*mdx* and 1,133 genes
775 upregulated for B10-*mdx*. Expression is z-score values of variance-stabilizing transformation
776 (VST) normalized data. **C.** Gene Ontology (GO) analysis performed using Cytoscape and
777 EnrichmentMap plugins to identify networks of related GO terms groups found upregulated (red
778 dots) in juvenile D2-*mdx* hearts relative to B10-*mdx.* Pink clusters refer to inflammatory-related
779 GO terms, while blue clusters refer to extracellular matrix-related GO terms. **D-E.** Boxplots
780 showing VST normalized gene expression levels for top 20 differentially expressed
781 inflammation-related (**D**; GOBP:Inflammatory Response) and extracellular matrix-related (**E**;
782 GOBP:External Encapsulating Structure) transcripts observed between juvenile D2-*mdx* and
783 B10-*mdx* hearts. Refer to Supplementary Fig. 3 for additional details.

784

785

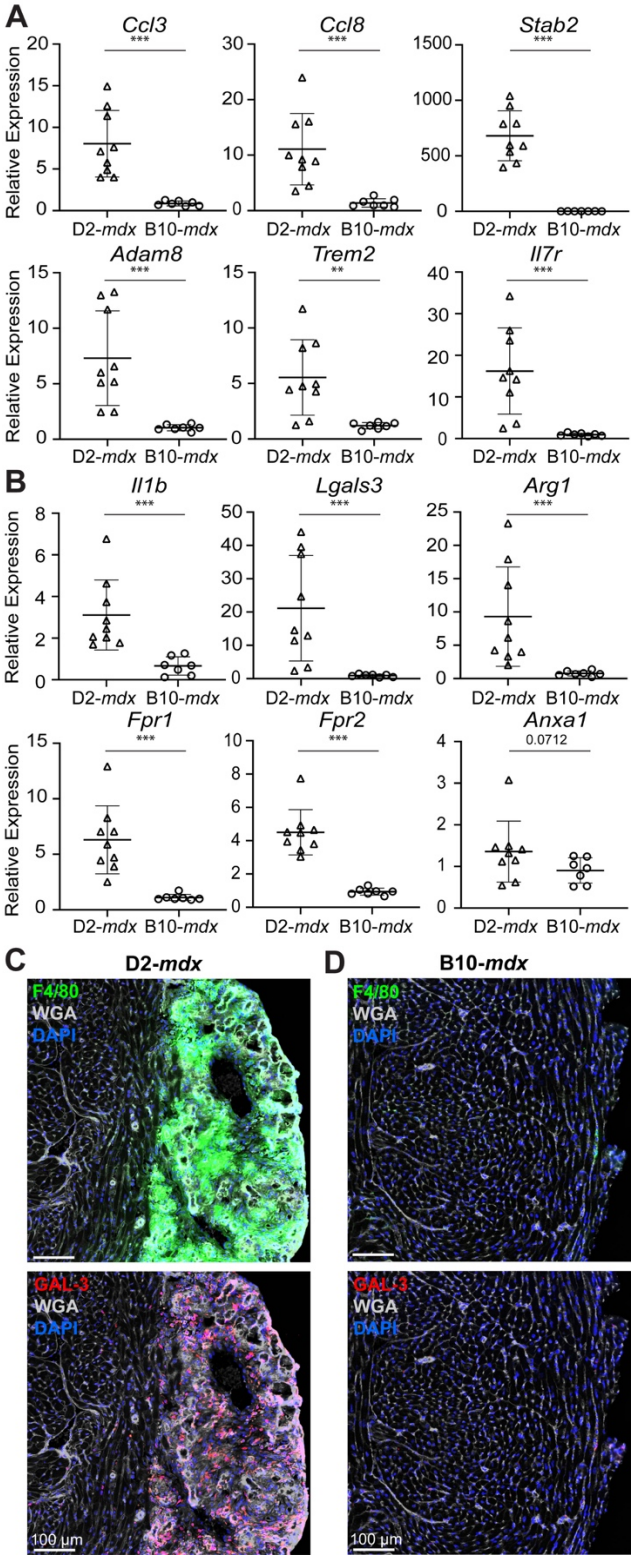

786

787 **Figure 3. Targeted analysis of inflammatory response at disease onset in D2-*mdx* B10-**

788 ***mdx* hearts. A.** qRT-PCR analysis of a distinct cohort of D2-*mdx* and B10-*mdx* hearts to assess

789 the expression of inflammatory genes identified by RNAseq analysis cohort to be differentially
790 expressed. Transcripts include top dysregulated genes involved in leukocyte activation,
791 migration and chemotaxis and regulation of inflammatory response and leukocyte-mediated
792 immunity (*Ccl3, Ccl8, Stab2, Adam8, Trem2, Il7r*). Relative gene expression values normalized
793 to internal *Hprt* transcript levels. **B.** qRT-PCR analysis of a distinct cohort of D2-*mdx* and B10-
794 *mdx* hearts to assess inflammatory genes that show broad dysregulation of neutrophil and
795 macrophage response in juvenile D2-*mdx* hearts. Relative gene expression values normalized
796 to internal *Hprt* transcript levels. **C-D.** Images showing immunostaining for pan-macrophage
797 marker, F4/80 (green), and pro-inflammatory, pathogenic macrophage marker, GAL-3 (red), in
798 juvenile D2-*mdx* (**C**) and B10-*mdx* (**D**). Data represent mean ± SD from $n = 7$-9 hearts per
799 cohort. Statistical analyses performed using Mann Whitney U test; *$p < 0.05$, **$p < 0.001$,
800 ***$p < 0.001$. For age-matched WT controls, refer to Supplementary Fig. 4.

801

802

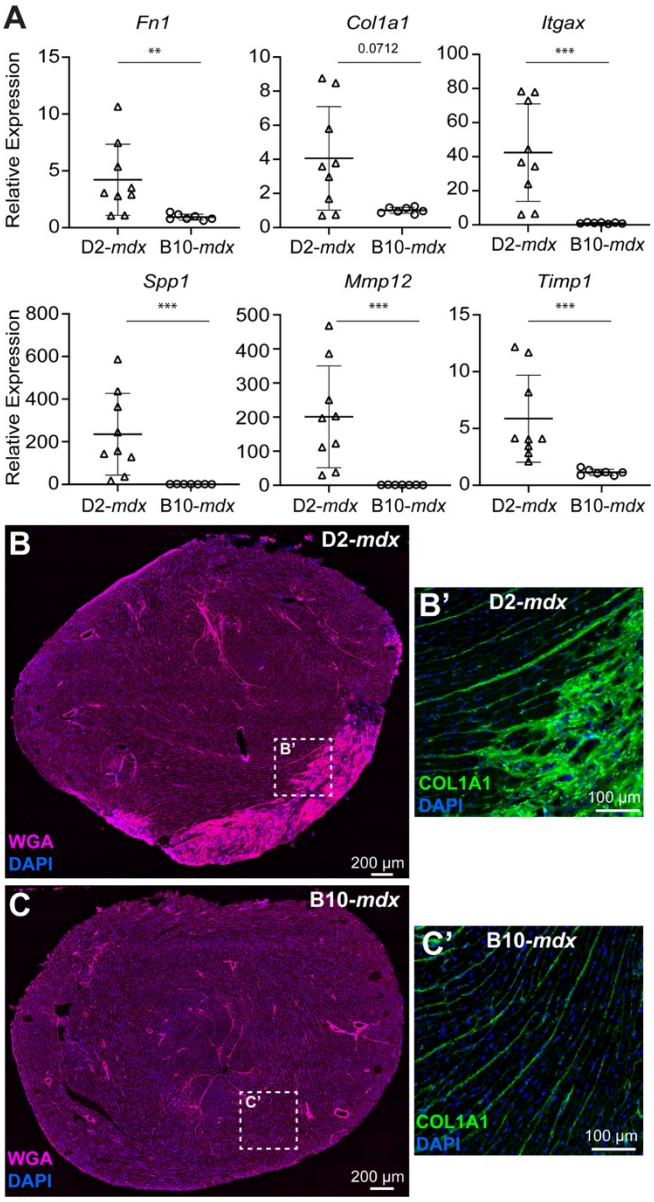

Figure 4. Targeted analysis of extracellular matrix remodeling response at disease onset in D2-*mdx* B10-*mdx* hearts. A. qRT-PCR analysis of a distinct cohort of D2-*mdx* and B10-*mdx* hearts to assess the expression of extracellular matrix-associated genes involved in matrix organization/re-organization (*Fn1, Col1a1, Itgax, Spp1, Mmp12, Timp1)* that are identified to be dysregulated by the RNAseq cohort. Relative gene expression values normalized to internal *Hprt* transcript levels. **B-C.** Images showing extracellular matrix distribution visualized using wheat germ agglutinin (WGA, pink) within, and surrounding, areas of cardiac damage in juvenile

811 D2-*mdx* (**B**), and B10-*mdx* (**C**). **B'-C'.** Zoom of the dotted area from whole cross-sectional

812 images showing immunostaining for COL1A1 within the extracellular matrix shows increased

813 COL1A1 expression in damaged D2-*mdx* hearts (**B'**), relative to B10-*mdx* (**C'**), indicative of

814 early-onset endomysial fibrosis. Data represent mean ± SD from $n = 7$-9 hearts per cohort.

815 Statistical analyses performed using Mann Whitney U test; *$p < 0.05$, **$p < 0.001$, ***$p < 0.001$.

816 For age-matched WT controls, refer to Supplementary Fig. 4.

817

818

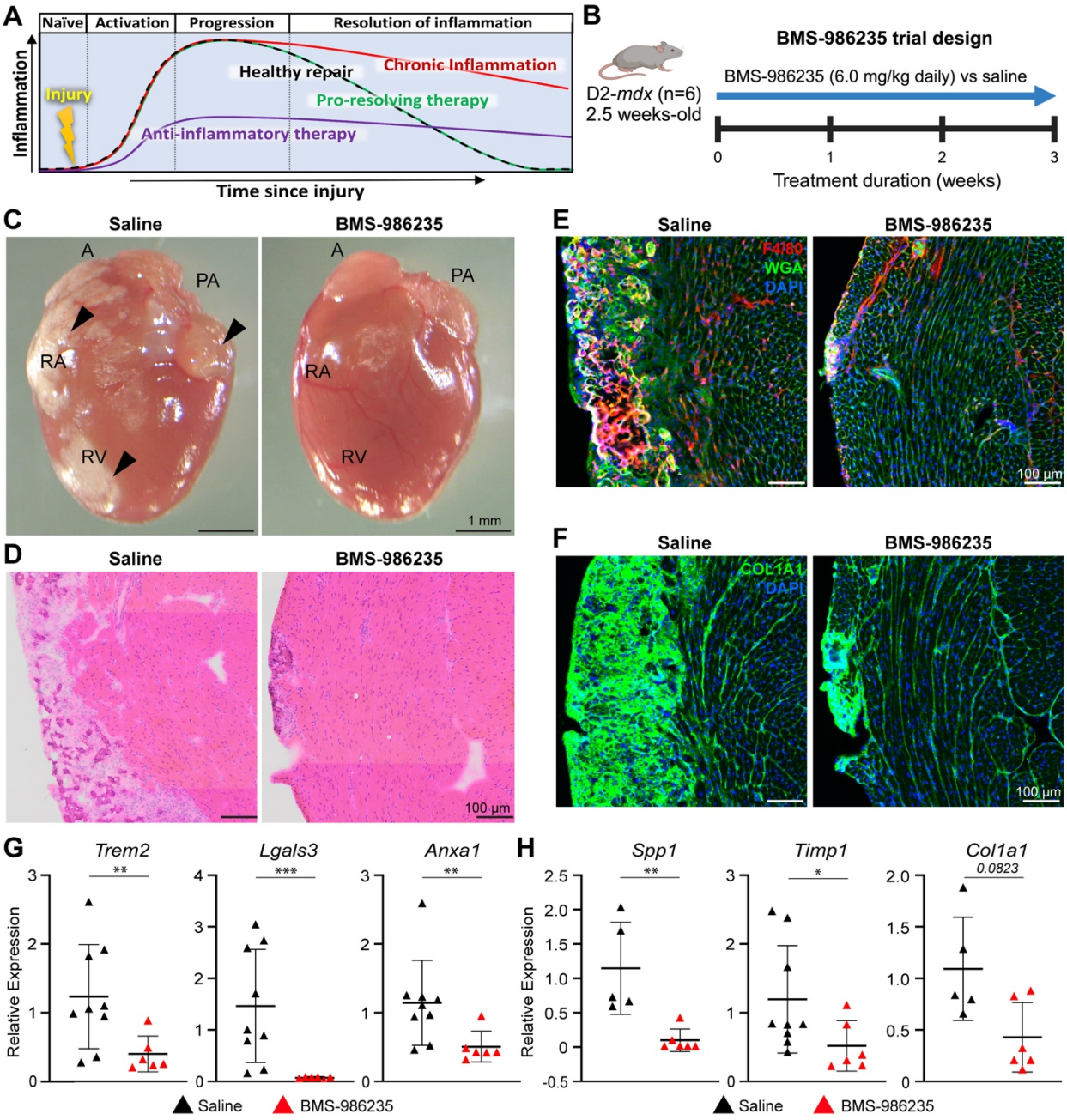

Figure 5. Pro-resolving therapy to mitigate cardiac disease onset in juvenile D2-*mdx*. A. Schematic describing the inflammatory response following cardiac injury in health (black trace) or dystrophic (red trace), showing acute versus chronic inflammation respectively. Use of anti-inflammatory drug (purple trace) lowers inflammatory response blunting inflammation, instead use of pro-resolving therapy (green trace) does not impact the onset of inflammation but helps clear inflammation preventing the inflammation to become chronic. **B.** Schematic detailing the

826 pre-clinical testing of pro-resolving drug, BMS-986235 (6.0mg/kg, 3 wk daily administration) in
827 D2-*mdx* mice (n=6) just prior to disease onset (18-19 days old). **C.** Whole tissue images of the
828 matched orientation of hearts showing ventricular and atrial fibro-calcified damage in saline or
829 BMS-986235-treated D2-*mdx* mice. **D.** Image showing cross-section of D2-*mdx* heart stained
830 for histological features by H&E from mice treated with saline or BMS-986235. **E.** Images
831 showing cross-section of D2-*mdx* heart immunostained for pan-macrophage marker, F4/80 (red)
832 and counterstained with WGA (green) and DAPI (blue) to mark the ECM and nuclei,
833 respectively. **F.** Image showing heart cross-section immunostained for COL1A1 and
834 counterstained with DAPI (blue) to visualize nuclei. **G-H.** qRT-PCR analysis of inflammatory (**G**)
835 and extracellular matrix genes (**H**) to assess the effect of drug treatment of D2-*mdx* mice (red
836 triangles), as compared with saline-treated controls (black triangles). Relative gene expression
837 values normalized to internal *Hprt* transcript levels. Data represent mean ± SD from $n = 6$ hearts
838 per cohort. Statistical analyses performed using Mann Whitney U test; *$p < 0.05$, **$p < 0.001$,
839 ***$p < 0.001$.
840
841
842
843
844

845 **Supplemental Material.**

846

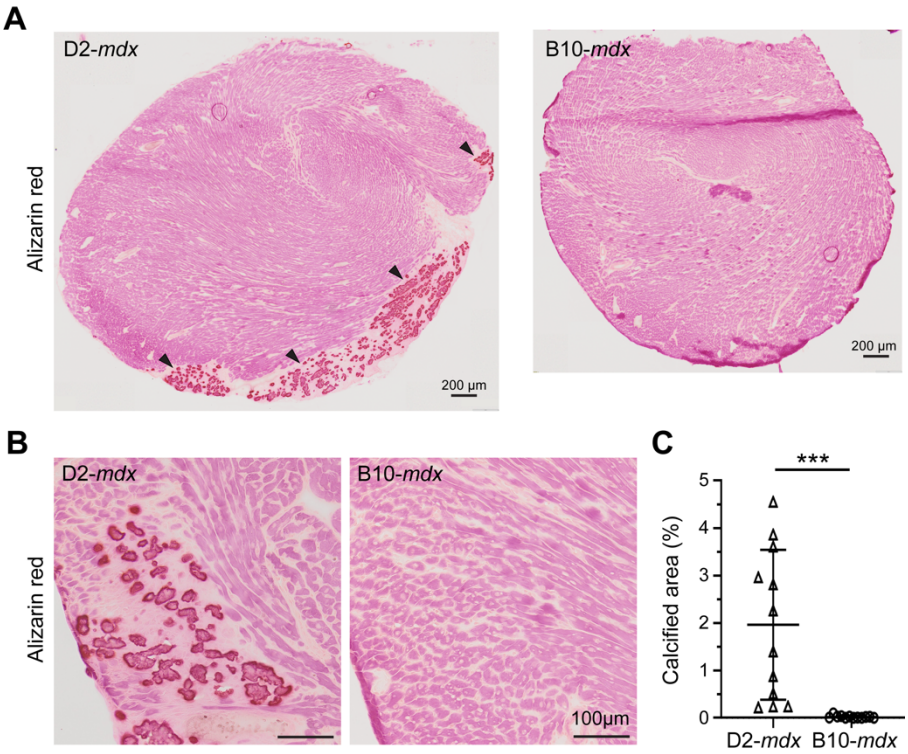

847

848

849 **Supplemental Figure 1. Cardiac histopathology in juvenile D2-*mdx* model. A.** Alizarin Red

850 staining of juvenile D2-*mdx* and B10-*mdx* hearts (whole cross-section) showing right ventricular

851 (RV) heart damage and calcification in juvenile D2-*mdx* hearts. Scale bars indicate 200µm. **B-C.**

852 High magnification images from panel A, showing Alizarin Red staining of juvenile D2-*mdx* and

853 B10-*mdx* hearts, and corresponding quantification of calcified fiber area per total tissue area. of

854 fibrosis, damage and calcification are highlighted by black arrowheads (**C**). Scale bars indicate

855 100µm. Statistical analyses performed using Mann Whitney U test; ***$p < 0.001$.

856

857

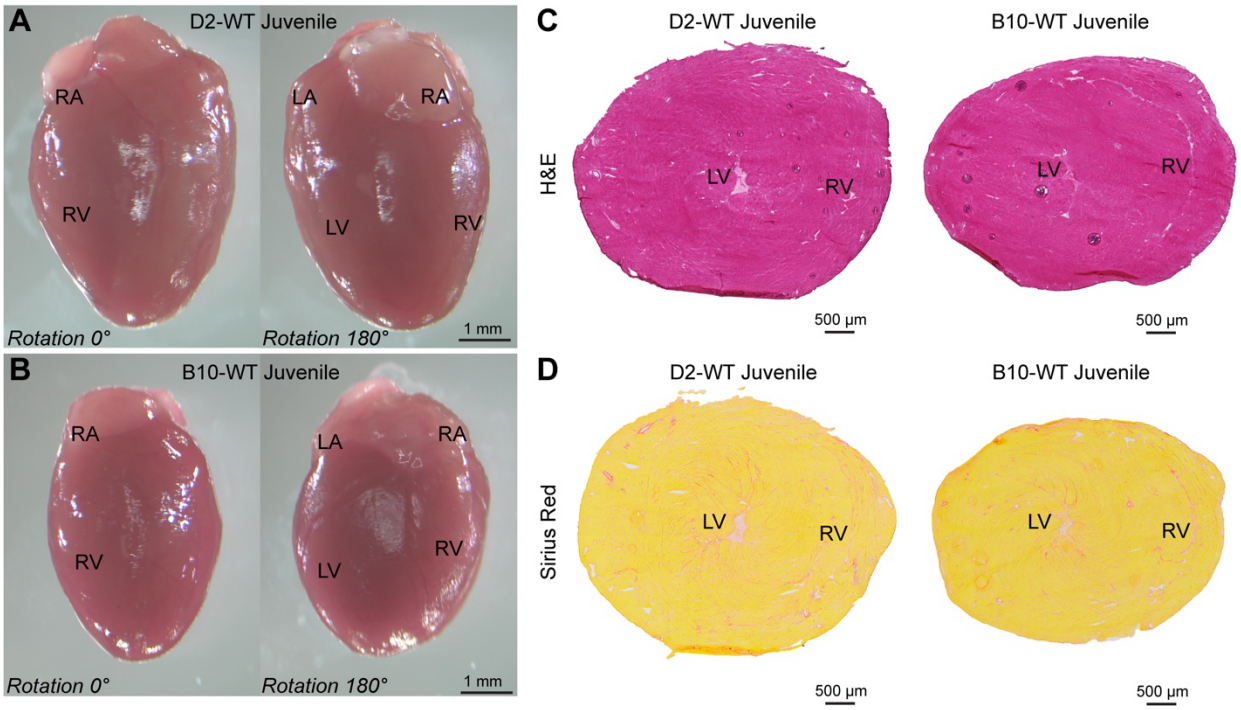

Supplemental Figure 2. Histopathological assessment of juvenile D2-WT and B10-WT hearts. Images show hearts harvested from juvenile (6 ± 0.5 wk) D2-WT and B10-WT mice. **A-B.** Whole tissue images with matched orientation of D2-WT (**A**) and B10-WT (**B**) hearts showing lack of any ventricular and atrial fibro-calcified damage. **C-D.** Cross-sectional images of juvenile D2-*mdx* and B10-*mdx* hearts through the ventricular lumen, stained for histological features by H&E (**C**), and for fibrosis by Sirius Red (**D**). Both D2-WT and B10-WT hearts lack any signs of fibro-calcified damage.

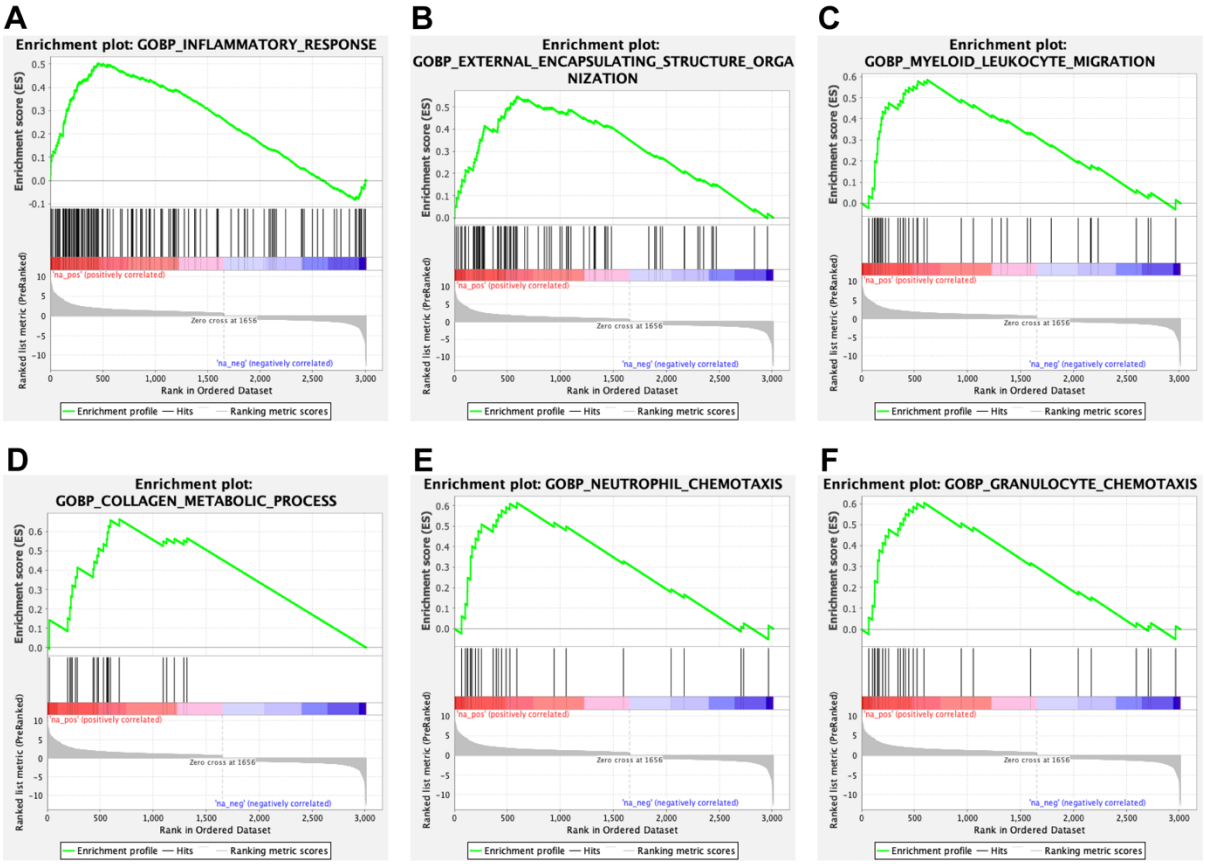

Supplemental Figure 3. GSEA enrichment plot analysis of top gene ontology (GO) hits from differential gene expression analysis in juvenile D2-*mdx* and B10-*mdx* hearts. A-F. Enrichment plot analysis of top immune-related (**A, C, E, F**) and extracellular matrix-related (**B, D**) GO biological process (BP) terms obtained using GSEA, including Inflammatory Response (**A**), Encapsulating Structure Organization (**B**), Myeloid Luekocyte Migration (**C**), Collagen Metabolic Process (**D**), Neutrophil Chemotaxis (**E**), and Granulocyte Chemotaxis (**F**).

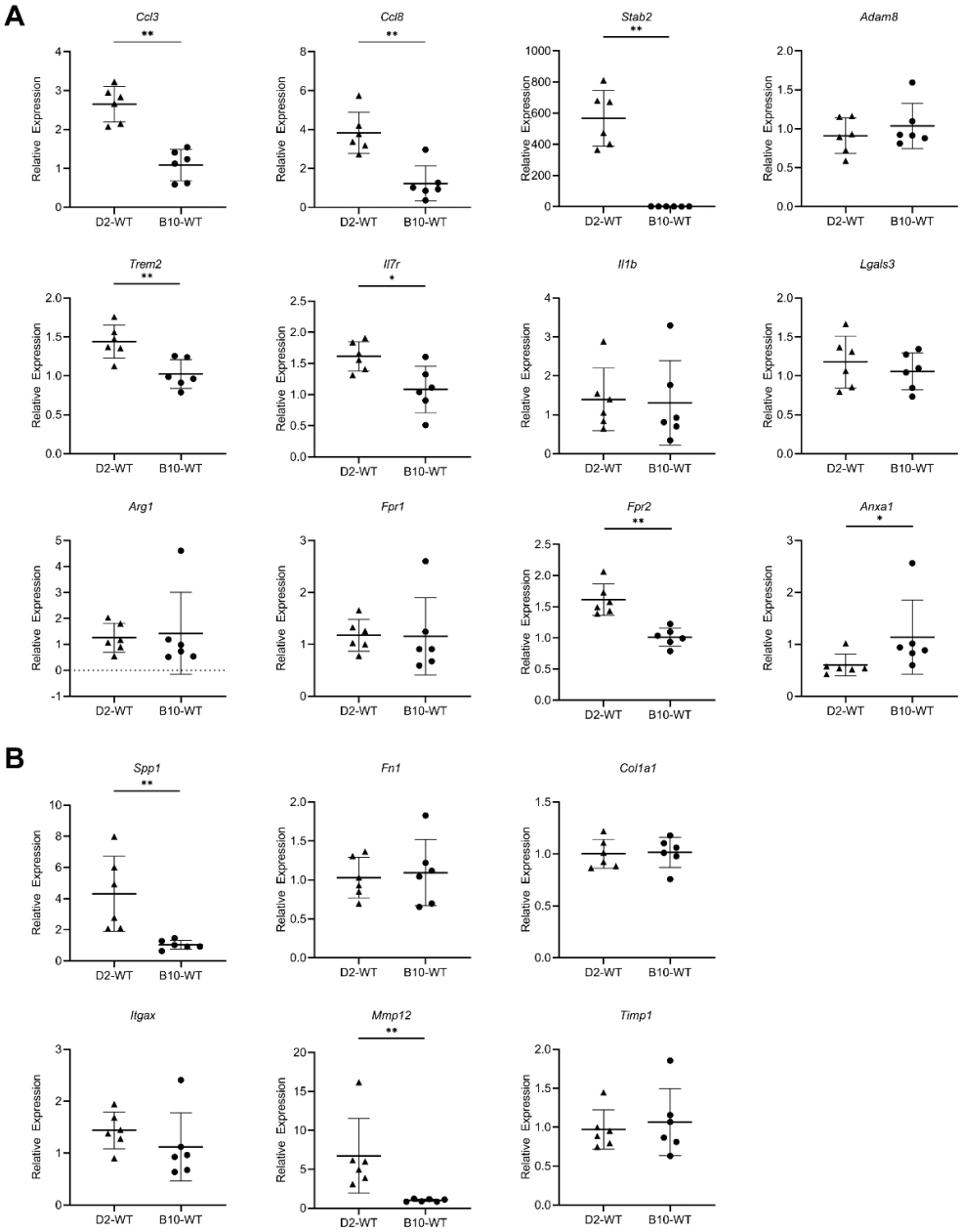

886

887 **Supplemental Figure 4. Gene expression analysis of D2-WT and B10-WT hearts for**

888 **selected immune and extracellular matrix targets. A.** Relative gene expression analysis for

889 dysregulated immune-related genes between D2-*mdx* vs. B10-*mdx* (**Figure 3**) assessed in

890 juvenile D2-WT and B10-WT hearts. **B.** Relative gene expression analysis for dysregulated

891 immune-related genes between D2-*mdx* vs. B10-*mdx* (**Figure 4**) assessed in juvenile D2-WT

892 and B10-WT hearts. Relative gene expression values normalized to internal *Hprt* transcript

893 levels.